

Modality Decoupling is All You Need: A Simple Solution for Unsupervised Hyperspectral Image Fusion

Songcheng Du¹ [†], Yang Zou^{1,4} [†], Zixu Wang¹, Xingyuan Li², Ying Li^{1*}, Qiang Shen^{3*}

¹ School of Computer Science, Northwestern Polytechnical University

² School of Software Technology, Dalian University of Technology

³ Institute of Mathematics, Physics and Computer Science, Aberystwyth University

⁴ The National Engineering Laboratory for Integrated Aero-Space-Ground-Ocean Big Data Application Technology, Northwestern Polytechnical University

{dusongcheng, archerv2, wangzixu0827}@mail.nwpu.edu.cn, xingyuan_lxy@163.com, lybyp@nwpu.edu.cn, qqs@aber.ac.uk

Abstract

*Hyperspectral Image Fusion (HIF) aims to fuse low-resolution hyperspectral images (LR-HSIs) and high-resolution multispectral images (HR-MSIs) to reconstruct high spatial and high spectral resolution images. Current methods typically apply direct fusion from the two modalities without valid supervision, failing to fully perceive the deep modality-complementary information and hence, resulting in a superficial understanding of inter-modality connections. To bridge this gap, we propose a simple and effective solution for unsupervised HIF with an assumption that modality decoupling is essential for HIF. We introduce the modality clustering loss that ensures clear guidance of the modality, decoupling towards modality-shared features while steering clear of modality-complementary ones. Also, we propose an end-to-end **Modality-Decoupled Spatial-Spectral Fusion (MossFuse)** framework that decouples shared and complementary information across modalities and aggregates a concise representation of the LR-HSI and HR-MSI to reduce the modality redundancy. Systematic experiments over multiple datasets demonstrate that our simple and effective approach consistently outperforms the existing HIF methods while requiring considerably fewer parameters with reduced inference time.*

1. Introduction

Hyperspectral imaging captures detailed reflectance data across a continuous spectrum, typically at narrow intervals (such as 10 nm). This capability enables precise mate-

rial differentiation based on spectral signatures, driving its widespread use in fields like natural resource management and remote sensing [26, 36, 52]. In the real world, however, optical systems typically offer either high spatial resolution with coarse spectral information (i.e., HR-MSI) or a greater number of spectral bands at lower spatial resolution (i.e., LR-HSI) due to the physical limitations of sensors [18, 19]. To improve the usability of hyperspectral images (HSIs), the fusion of observed LR-HSI and HR-MSI has emerged as an efficient and promising method, drawing considerable attention [40, 44].

Without losing generality, HR-MSI and LR-HSI can be considered as the spatial and spectral degradation of high-resolution hyperspectral image (HR-HSI), respectively [12, 39]. The related observation models can be mathematically expressed as $Y = XR$ and $x = CX$, where $X \in \mathbb{R}^{H \times W \times B}$, $Y \in \mathbb{R}^{H \times W \times b}$ and $x \in \mathbb{R}^{h \times w \times B}$ represent the target HR-HSI, the HR-MSI and the LR-HSI, respectively. Here, $H(h)$, $W(w)$ and $B(b)$ denote the height, width, and number of bands of images, respectively, where $h \ll H$, $w \ll W$, $b \ll B$. The matrix $R \in \mathbb{R}^{B \times b}$ represents the spectral response function (SRF), and $C \in \mathbb{R}^{hw \times HW}$ represents the point spread function (PSF) which is often modeled as a convolution with a blur kernel K followed by a spatial downsampling operation.

Recently, numerous methods have been proposed to address this ill-posed problem, which can be categorized into three types, as illustrated in Fig. 1. In (I), the matrix factorization-based techniques facilitate information fusion through linear transformations. In (II), the coupled branch architectures address the information deficiency in each modality by employing a multi-step cross-fusion process, which independently enhances both modalities. In (III), the repetitive integration approach combines observed LR-

[†]These authors contributed equally to this work

*Corresponding author

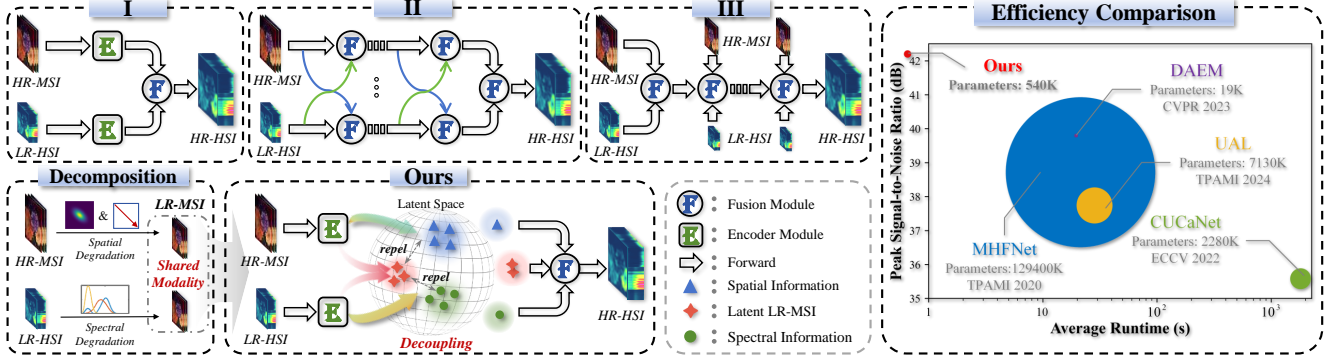


Figure 1. Algorithmic core difference with existing HIF methods (I, II, and III) and efficiency comparison of our proposed MossFuse. We propose and validate the assumption that **the modality decoupling is essential for unsupervised HIF**. As a result, our simple solution significantly outperforms the existing HIF methods while requiring considerably lower parameters with reduced inference time.

HSI and HR-MSI with a main branch to prevent information loss. These architectures generally require the independent extraction of spatial and spectral feature representations from HR-MSI and LR-HSI prior to fusion. However, two major challenges persist: 1) **Overlooking the deep modality-complementary information**, where the direct fusion of two modalities without valid supervision fails to adequately capture the deep modality-complementary information across modalities. This leads to redundant features and the deterioration of valuable modality-specific characteristics, ultimately yielding suboptimal fusion results. 2) **Reduced efficiency**, as the repeated extraction of redundant features increases computational costs. Given those limitations, we ask, **“Is it possible to learn only the essential modality-complementary information through modality decoupling, rather than relying on direct fusion?”**

The answer is yes. We found that the latent low-resolution multispectral image (LR-MSI) serves as the modality-shared component between HR-MSI and LR-HSI. Therefore, we come up with the assumption that **the modality decoupling is essential for unsupervised HIF**. As shown in Fig. 1(Decomposition), the LR-MSI can be obtained from both spatial degradation on HR-MSI Y and spectral degradation on LR-HSI x . Inspired by this observation, we propose a simple and effective solution for unsupervised HIF that reconstructs a finer HR-HSI image with significantly lower parameters and inference time.

First, we propose an end-to-end modality-decoupled spatial-spectral fusion framework, MossFuse, to establish the foundation of our assumption. Specifically, we build a coarse-to-fine multi-modality decoupling process to decouple the LR-HSI and HR-MSI into modality-complementary and modality-shared components in the latent space. The proposed modality reconstruction process then aggregates these concise representations of modalities to reconstruct the desired HR-HSI. Moreover, we establish a modality constraint process to secure the modality decoupling effi-

cacy by constraining the reversibility of the multi-modality decoupling process in a self-supervised manner.

Furthermore, a degradation estimation process is also developed to accurately determine degradation parameters, enabling effective handling of unsupervised scenarios.

Subsequently, we formulate our assumption by introducing a modality clustering loss, which guides the model in disentangling modality-shared and modality-complementary information from HR-MSI and LR-HSI. This loss compels the multi-modality decoupling process to aggregate the shared LR-MSI information from both HR-MSI and LR-HSI while simultaneously distinguishing it from their modality-complementary spatial and spectral components. Our objective is to prove that simply fusing the thoroughly decoupled modality-shared LR-MSI and modality-complementary spatial and spectral information indeed enhances fusion performance without the need for complex network architecture or vast parameters, leading to a finer HR-HSI with significantly fewer parameters and reduced inference time.

To this end, we propose MossFuse for unsupervised hyperspectral image fusion (HIF) tasks, emphasizing the significance of modality decomposition. Our contributions are summarized as follows:

- We propose a simple and effective solution for HIF based on our assumption: modality decoupling is essential for hyperspectral image fusion. To the best of our knowledge, this is the first work to solve HIF from a modality decomposition perspective.
- We introduce a modality clustering loss to guide the fusion processes, aggregating the shared LR-MSI components while discerning them from the modality-complementary spatial and spectral components.
- We develop an end-to-end modality-decoupled spatial-spectral fusion framework that decouples the shared and complementary information across modalities while aggregating the concise representation of the HSI and MSI

to reduce the modality redundancy.

- We present systematic experimental results validating our assumption and approach. Our simple and effective approach outperforms the existing HIF methods across five popularly used datasets while requiring considerably lower parameters with reduced inference time.

2. Related Work

2.1. Linear Decomposition based Fusion

Fusion methods using linear decomposition typically decompose high-resolution multispectral images (HR-MSIs) and low-resolution hyperspectral images (LR-HSIs) to extract spatial and spectral features [7, 10, 23, 32]. These methods can be broadly classified into matrix and tensor factorization paradigms [22, 43, 47]. The matrix factorization method assumes that each pixel in an HSI is a linear combination of a finite set of reflectances. Kawakami et al. [15] initially applied an unmixing technique to estimate basis reflectance spectra from LR-HSI and subsequently used the coefficients obtained from HR-MSI to achieve the desired outcomes based on a sparse prior. Unlike matrix factorization, tensor factorization directly decomposes an HR-HSI scene into a core tensor and dictionaries corresponding to the spatial and spectral dimensions. For instance, Dian et al. [5] used Tucker decomposition to capture non-local and coupled structural information, respectively. Kanatsoulis et al. [14] applied Canonical Polyadic (CP) decomposition to decompose the high-resolution hyperspectral image (HR-HSI), estimating each factor matrix via least squares. However, in real-world environments, multiple light interactions with surfaces complicate linear representations, causing the solution to diverge from the true one.

2.2. Deep Learning based Fusion

Deep learning techniques, known for their ability to automatically capture the underlying structure of data, have inspired neural network-based fusion methods [4, 24, 28, 29, 31, 54]. Like linear decomposition approaches, many recent deep learning-based networks use a dual-branch autoencoder architecture to separately extract spatial and spectral information [45]. Qu et al. [30] pioneered a deep learning-based unsupervised fusion network that incorporates a Dirichlet distribution-induced layer within a multi-stage alternating optimization process. Yao et al. [45] improved the interpretability of their network by incorporating spectral unmixing theory into a coupled-autoencoder framework, using cross-fusion layers to exchange spatial and spectral information. Later, to improve adaptability to different samples, some methods incorporate Test-Time Adaptation (TTA), fine-tuning the network on test data. Zhang et al. [51] proposed an unsupervised adaptation learning (UAL) framework that first learned a general image using

deep networks and then adapted it to a specific HSI. Guo et al. [9] proposed a coordination optimization framework to estimate the desired HSI and its degradation, along with a partial fine-tuning strategy to cut computational costs, despite being time-consuming and having poor generalization.

3. The Proposed Method

3.1. Method Overview

As illustrated in Fig. 2(a), the main pipeline of our proposed modality-decoupled spatial-spectral fusion framework primarily comprises four components: multi-modality decoupling, modality reconstruction, modality constraint, and degradation estimation.

Given a high-resolution multispectral image (HR-MSI, denoted as Y) and a low-resolution hyperspectral image (LR-HSI, denoted as x) as two inputs, we first employ a multi-modality decoupling process to separate them into modality-complementary and modality-shared components in the latent space, guided by a modality clustering loss. Then, with the modality-shared and modality-complementary well clustered, we employ a modality reconstruction process to reconstruct the desired high-resolution hyperspectral image (HR-HSI, denoted as \hat{X}) by aggregating information from different modalities. Subsequently, we impose a self-supervised learning strategy to constrain the completeness and fidelity of the decoupled modalities by leveraging the modality aggregation operations. In addition, we accurately estimate the spatial and spectral degradation parameters based on the degradation models of HR-MSI and LR-HSI to alleviate the ill-posed unsupervised hyperspectral image fusion (HIF) task.

3.2. Multi-Modality Decoupling

We build a simple multi-modality decoupling process to decouple the LR-HSI and HR-MSI into modality-complementary and modality-shared components in the latent space. We first employ base feature encoders to extract the shallow feature of the two inputs Y and x . Each base feature encoder is equipped with four spectral-wise transformer (SWT) blocks [50] to obtain F_Y^B and F_x^B , respectively. Specifically, the SWT comprises a spectral-wise self-attention (SWSA), a feed-forward network, and two layer normalization operations.

To establish our assumption, we then propose three types of modality encoders to decompose F_Y^B and F_x^B into four parts: a modality-complementary spatial component F_Y^C , a modality-complementary spectral component F_x^C and two modality-shared components F_Y^S and F_x^S , formulated as $F_Y^B = F_Y^S \oplus F_Y^C$ and $F_x^B = F_x^S \oplus F_x^C$.

First, we utilize the LK-CNN block [53] as the spatial-modality encoder to extract modality-complementary spatial features from the HR-MSI (Y). The LK-CNN block

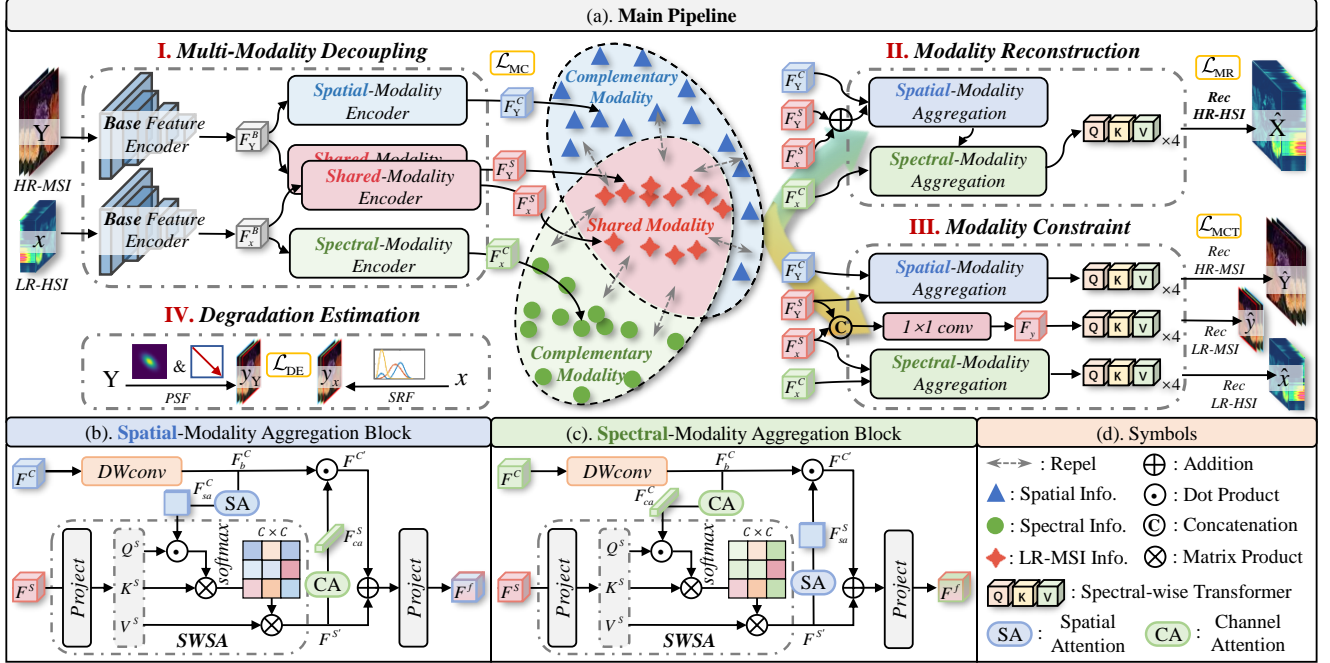


Figure 2. The architecture of MossFuse. (a) The main pipeline, consisting of four key components: **I.** Multi-Modality Decoupling, **II.** Modality Reconstruction, **III.** Modality Constraint, and **IV.** Degradation Estimation. The losses associated with each component are denoted as follows: \mathcal{L}_{MC} (modality clustering loss), \mathcal{L}_{MR} (modality reconstruction loss), \mathcal{L}_{MCT} (modality constraint loss), and \mathcal{L}_{DE} (degradation estimation loss). (b) and (c) show the detailed architecture of the Spatial- and Spectral- Modality Aggregation Blocks, respectively.

captures broad spatial information through the use of a few large kernels rather than layering numerous small kernels, thereby improving the model’s efficiency and performance without increasing network depth. Subsequently, we employ an SWT block as the spectral-modality encoder to capture modality-complementary spectral characteristics from LR-HSI (x). The SWT block treats each spectral feature as a token, applying self-attention along the spectral dimension to efficiently extract features within the spectral domain. Additionally, two shared modality encoders comprising an LK-CNN block and an SWT block are used to extract the modality-shared low-resolution multispectral image (LR-MSI, denoted as y) components.

Moreover, the detailed architecture of SWT and LK-CNN are provided in the Supplementary Materials.

3.3. Modality Reconstruction

With the modality-shared and modality-complementary components from the HR-MSI and LR-HSI effectively decoupled, we proceed to the modality reconstruction phase to reconstruct the desired HR-HSI (\hat{X}) by integrating these components. Starting with the modality-shared information, we progressively incorporate complementary spatial and spectral information. This process refines cross-attention in the spatial and spectral aggregation blocks using gate-like mechanisms and residual connections.

Recall that F_Y^S and F_x^S represent the same modality information, we first combine these shared components and aggregate the spatial complementary information from F_Y^C through the spatial-modality aggregation block, denoted as $\Phi_{\theta_x}^{spa}(\cdot, \cdot)$. Following this, the spectral complementary information F_x^C is then integrated by using the spectral-modality aggregation block, denoted as $\Phi_{\theta_x}^{spe}(\cdot, \cdot)$. Thus, the latent feature of the HR-HSI can be formulated as: $F_X = \Phi_{\theta_x}^{spe}(\Phi_{\theta_x}^{spa}(F_Y^S + F_x^S, F_Y^C), F_x^C)$.

Ultimately, the desired HR-HSI (\hat{X}) is reconstructed via the decoder $\mathcal{D}_{\theta_x}(\cdot)$, which incorporates four SWT blocks. Formally, this can be expressed as $\hat{X} = \mathcal{D}_{\theta_x}(F_X)$.

Notably, both the spatial-modality and spectral-modality aggregation blocks employ the spectral-wise self-attention (SWSA) framework. Each incorporates a parallel convolutional branch with a gate-like mechanism that dynamically adjusts feature weighting across spatial and channel dimensions, enabling efficient fusion of the two input features.

Spatial-Modality Aggregation Block. As shown in Fig. 2(b), given the modality-shared feature F^S and modality-complementary spatial feature F_Y^C as inputs, we first apply linear transformations to F^S , obtaining the query Q^S , key K^S , and value V^S . Simultaneously, for the convolutional branch, a depth-wise convolution (DW-Conv) is applied to F_Y^C to derive the base feature F_b^C . Leveraging the spatial attention (SA) mechanism [3, 11], we then extract

a spatial attention map $F_{sa}^C \in \mathbb{R}^{H \times W \times 1}$ from F_b^C . The spatial interaction between the two branches is achieved through a dot product with the query Q^S , expressed as $Q^{SC} = SA(F_b^C) \odot Q^S$, where Q^{SC} denotes the spatially enhanced output and $SA(\cdot)$ the spatial attention operation. The output of the SWSA branch is computed as $F^{S'} = V^S \cdot \text{softmax}((Q^{SC})^T K^S / d)$, where d is a learnable temperature parameter.

To achieve comprehensive fusion of the two modalities, we extract a channel attention map $F_{ca}^S \in \mathbb{R}^{1 \times 1 \times N}$ from $F^{S'}$ using the channel attention (CA) mechanism [11], where N is the number of channels. This channel map is then used to perform a dot product with F_b^C to obtain the output of the convolutional branch $F^{C'}$, formally: $F^{C'} = CA(F^{S'}) \odot F_b^C$. Finally, the fused feature F^f of the two modalities is obtained by adding $F^{S'}$ and $F^{C'}$, and through a linear projection operation.

Spectral-Modality Aggregation Block. As shown in Fig. 2(c), similar to the two-branch architecture in the spatial-modality aggregation block, we map the modality-shared feature F^S into Q^S , K^S , and V^S representations through linear transformations. Concurrently, we apply a DW-Conv to the modality-complementary spectral feature F_Y^C to extract the base feature F_b^C .

To derive spectral details from F_b^C and enhance the shared features, we leverage the CA mechanism [11] to compute the channel attention map $F_{ca}^C \in \mathbb{R}^{1 \times 1 \times N}$ from F_b^C , followed by a dot product operation with the query Q^S . This process can be expressed as $Q^{SC} = CA(F_b^C) \odot Q^S$, where Q^{SC} denotes the spectrally enhanced output and $CA(\cdot)$ the channel attention operation. Similarly, the output of the SWSA branch, following the structure in the spatial-modality aggregation block, is denoted as $F^{S'}$.

Moreover, we compute a spatial attention map $F_{sa}^S \in \mathbb{R}^{H \times W \times 1}$ from $F^{S'}$ and apply a dot product with F_b^C to sufficiently fuse the two modalities, producing the output $F^{C'}$ of the convolutional branch: $F^{C'} = SA(F^{S'}) \odot F_b^C$. The final fused feature F^f is then obtained by adding $F^{S'}$ and $F^{C'}$, and through a linear projection operation.

In addition, the detailed architecture of SWSA, $SA(\cdot)$ and $CA(\cdot)$ are given in the Supplementary Materials.

3.4. Modality Constraint

To ensure the completeness and fidelity of the decoupled modalities information, we apply a self-supervised learning strategy that leverages modality aggregation operations.

Specifically, we employ the spatial-modality aggregation block $\Phi_{\theta_Y}^{spa}(\cdot, \cdot)$ and the spectral-modality aggregation block $\Phi_{\theta_x}^{spe}(\cdot, \cdot)$ to recover the original HR-MSI Y and LR-MSI x from the decoupled representations F_Y^C , F_Y^S , F_x^C , and F_x^S , formally:

$$F_Y = \Phi_{\theta_Y}^{spa}(F_Y^C, F_Y^S), \quad \text{and} \quad F_x = \Phi_{\theta_x}^{spe}(F_x^C, F_x^S). \quad (1)$$

Moreover, to constrain the two modality-shared representations F_Y^S and F_x^S , we concatenate them along the channel dimension and apply a 1×1 convolution, yielding the representation F_y of the LR-MSI.

Finally, the three aggregated representations are decoded by their respective decoders $\mathcal{D}_{\theta_i}(\cdot)$, where $\mathcal{D}_{\theta_i}(\cdot)$ denotes a decoder parameterized by θ_i , with $i \in \{Y, x, y\}$. Each decoder produces the following outputs: $\hat{Y} = \mathcal{D}_{\theta_Y}(F_Y)$, $\hat{x} = \mathcal{D}_{\theta_x}(F_x)$, and $\hat{y} = \mathcal{D}_{\theta_y}(F_y)$.

3.5. Degradation Estimation

To alleviate the ill-posed nature of the unsupervised HIF task, we accurately estimate the spatial and spectral degradation parameters.

Spatial Degradation Estimation. Numerous studies suggest that the spatial-wise degradation of real-world scenarios can be approximated with anisotropic Gaussian kernels (AGK) [8, 37, 48]. Accordingly, we simulate the point spread function (PSF), denoted as C , following this approach. To be specific, an AGK is characterized by three parameters: λ_1 and λ_2 , which represent the eigenvalues of the kernel, and θ_K , the rotation angle. The covariance matrix of the kernel is calculated as follows:

$$\Sigma = \begin{bmatrix} \cos \theta_K & -\sin \theta_K \\ \sin \theta_K & \cos \theta_K \end{bmatrix} \begin{bmatrix} \lambda_1 & 0 \\ 0 & \lambda_2 \end{bmatrix} \begin{bmatrix} \cos \theta_K & \sin \theta_K \\ -\sin \theta_K & \cos \theta_K \end{bmatrix}.$$

Further, the AKG-based blur kernel can be expressed as $K = F_K(\Sigma)$, where F_K is a function that generates the values of a 2D kernel based on kernel parameters [48].

Spectral Degradation Estimation. The complexity of material properties often makes it challenging to accurately represent spectral response functions (SRF) with simple mathematical formulas [21, 25, 27]. Therefore, we model the SRF using a 1×1 convolutional operation that integrates various physical constraints.

Specifically, we apply clamped activation at each iteration to ensure parameter non-negativity. Additionally, a normalization operator is used to satisfy the sum-to-one constraint for the SRF across the spectral dimension.

3.6. Network Optimization

Modality Clustering Loss. Inspired by the assumption, we proposed a modality clustering loss to guide the multi-modality decoupling, aggregating the shared LR-MSI information while distinguishing it from modality-complementary spatial and spectral ones. Recall that the multi-modality decoupling process decomposes the HR-MSI (Y) and LR-MSI (x) into four components: a modality-complementary spatial component F_Y^C , a modality-complementary spectral component F_x^C and two modality-shared components F_Y^S and F_x^S . We define $f(a, b) = \exp^{\cos(a, b)}$ as the latent space similarity metric, measuring the cosine similarity loss between a and b . The contrastive modality clustering loss \mathcal{L}_{MC} is computed by:

$$\mathcal{L}_{MC} = -\log \frac{f(F_Y^S, F_x^S)}{\sum_{i \in \{Y, x\}} f(F_i^S, F_i^C) + \sum_{m \in \{S, C\}} f(F_Y^m, F_x^m)}. \quad (2)$$

The modality clustering loss \mathcal{L}_{MC} substantiates our assumption by encouraging the network to accurately aggregate shared LR-HSI components while distinguishing modality-complementary spatial and spectral features. This reduces modality redundancy and enhances fusion results.

Modality Reconstruction Loss. To reconstruct the desirable HR-HSI \hat{X} without ground truth, we utilize the degradation model of the HSI along with the estimated spatial and spectral degradation parameters SRF (R) and PSF (C). The modality reconstruction loss is formulated as:

$$\mathcal{L}_{MR} = \|Y - \hat{X}R\|_1 + \|x - C\hat{X}\|_1, \quad (3)$$

where $\|\cdot, \cdot\|$ represents the L1 loss.

Modality Constraint Loss. We propose the modality constraint loss \mathcal{L}_{MCT} to preserve the integrity and fidelity of the decoupled modality information. We first incorporate two inputs HR-MSI (Y) and LR-HSI (x) as supervisory items to form the \mathcal{L}_{MCT1} , ensuring the reversibility of the separated modalities, formally:

$$\mathcal{L}_{MCT1} = \|Y - \hat{Y}\|_1 + \|x - \hat{x}\|_1. \quad (4)$$

We also apply \mathcal{L}_{MCT2} on the decoded LR-MSI \hat{y} to guide the modality decoupling. Recall the LR-MSI can be obtained from both spatial degradation on HR-MSI Y and spectral degradation on LR-HSI x , denoted as y_Y and y_x , respectively. Therefore, we construct the \mathcal{L}_{MCT2} as:

$$\mathcal{L}_{MCT2} = \|y_Y - \hat{y}\|_1 + \|y_x - \hat{y}\|_1 = \|CY - \hat{y}\|_1 + \|xR - \hat{y}\|_1. \quad (5)$$

Thus, \mathcal{L}_{MCT} can be obtained by the combination of the above terms, expressed as: $\mathcal{L}_{MCT} = \mathcal{L}_{MCT1} + \mathcal{L}_{MCT2}$.

Degradation Estimation Loss. Based on the two LR-MSIs y_Y and y_x , which are generated by degradation from two inputs Y and x , respectively, we formulate the degradation estimation loss \mathcal{L}_{DE} to effectively supervise the spatial and spectral degradation parameters:

$$\mathcal{L}_{DE} = \|y_Y - y_x\|_1 = \|CY - xR\|_1. \quad (6)$$

Overall, the total training loss of the proposed MossFuse, comprising the aforementioned loss terms, formally:

$$\mathcal{L}_{total} = \mathcal{L}_{MC} + \mathcal{L}_{MR} + \mathcal{L}_{MCT} + \mathcal{L}_{DE}. \quad (7)$$

4. Experiment

4.1. Experiment Setup

Dataset. In this study, we used three synthetic hyperspectral image (HSI) datasets: CAVE [46], Harvard [2], and

NTIRE2018 [1], and two real HSI datasets: NCALM [42] and WV-2 [20] for evaluation. The CAVE dataset has 32 indoor images (31 bands, 400–700 nm, 512×512 pixels); Harvard has 50 outdoor samples (31 bands, 420–720 nm, 1392×1040 pixels); NTIRE2018 includes 54 training and 5 testing images (31 bands, 400–700 nm, 1392×1300 pixels). For real datasets, NCALM features 48 bands (380–1050 nm, 1202×4172 pixels) with a 3-band MSI (24040×83440 pixels), and WV-2 provides 8-bands HSI (418×685 pixels) with a 3-band MSI (1677×2633 pixels).

In training, we use 20 pairs from CAVE and 30 from Harvard, with the rest for testing. Synthetic high-resolution multispectral image (HR-MSI) and high-resolution hyperspectral image (LR-HSI) are generated using six spectral response curves [13] and Gaussian blur kernels. For NCALM and WV-2, following [20], we use the top halves for training, with testing on the bottom halves. Moreover, to create the training inputs, downsampling operations (factors 4 and 20) are employed per the Wald protocol [35].

Compared Method. For comparison, we select three tradition-based algorithms (including CSU [17], NSSR [6] and HySure [33]) and four state-of-the-art (SOTA) unsupervised fusion algorithms (including MHF [41], CUCaNet[45], UAL [51] and DAEM [9]).

Evaluation Measures. To comprehensively assess the effectiveness of the proposed method, four standard quantitative metrics are adopted [20]: the peak signal-to-noise ratio (PSNR), the structural similarity index (SSIM) [38], the spectral angle mapper (SAM) [49], and the relative dimensionless global error in synthesis (ERGAS) [34].

4.2. Implementation Details

Our algorithm is developed in Pytorch and runs on an NVIDIA 3090Ti GPU. For optimizing the parameters, we use the Adam optimizer [16] with $\beta_1 = 0.9$, $\beta_2 = 0.999$, and $\epsilon = 10^{-8}$, and implement a cosine annealing schedule to decay the learning rate from 10^{-3} to 10^{-6} .

4.3. Performance Comparison

Table 1 shows average reconstruction results across six degradation settings for the CAVE, Harvard, and NTIRE2018 datasets, where our algorithm outperforms others across all validation metrics, demonstrating its superior performance. Moreover, Fig. 3, and Fig. 4 illustrate the visual performance of various algorithms on the CAVE and NTIRE2018 datasets, with our reconstructions closely matching the ground truth.

For real datasets NCALM and WV-2, without HR-HSI for quantitative comparison, thus we can only rely on visual comparisons. Fig. 5 shows synthetic pseudo-RGB images extracted from HSI, where our method exhibits better detail and global context compared to others.

Datasets	CAVE [46]				Harvard [2]				NTIRE2018 [1]			
	PSNR \uparrow	SSIM \uparrow	SAM \downarrow	ERGAS \downarrow	PSNR \uparrow	SSIM \uparrow	SAM \downarrow	ERGAS \downarrow	PSNR \uparrow	SSIM \uparrow	SAM \downarrow	ERGAS \downarrow
CSU [17]	30.59	0.899	14.17	1.53	36.08	0.937	10.93	0.85	21.48	0.819	1.95	2.57
NSSR [6]	28.55	0.904	12.26	1.94	30.97	0.897	12.45	1.66	21.43	0.682	9.12	2.87
HySure [33]	27.63	0.841	16.63	4.01	35.67	0.880	8.35	0.84	12.99	0.577	3.20	8.47
MHFNet [41]	38.72	0.966	6.90	1.94	39.25	0.942	6.91	0.72	43.65	0.991	1.85	0.20
CUCaNet[45]	35.58	0.927	10.38	0.98	37.56	0.938	7.52	0.69	39.69	0.983	4.77	0.48
UAL [51]	37.74	0.974	9.28	0.70	40.95	0.952	7.29	0.66	44.79	0.996	1.34	0.08
DAEM [9]	<u>39.80</u>	<u>0.982</u>	<u>6.78</u>	<u>0.55</u>	<u>42.66</u>	<u>0.970</u>	<u>4.09</u>	<u>0.45</u>	<u>46.68</u>	<u>0.997</u>	<u>0.98</u>	<u>0.05</u>
Ours	42.05	0.990	6.57	0.42	44.52	0.992	3.89	0.39	48.53	0.999	0.79	0.04

Table 1. Average quantitative comparison of different methods on three synthetic datasets under six group degradations. The best results are in **bold**, while the second-best results are in underlined.

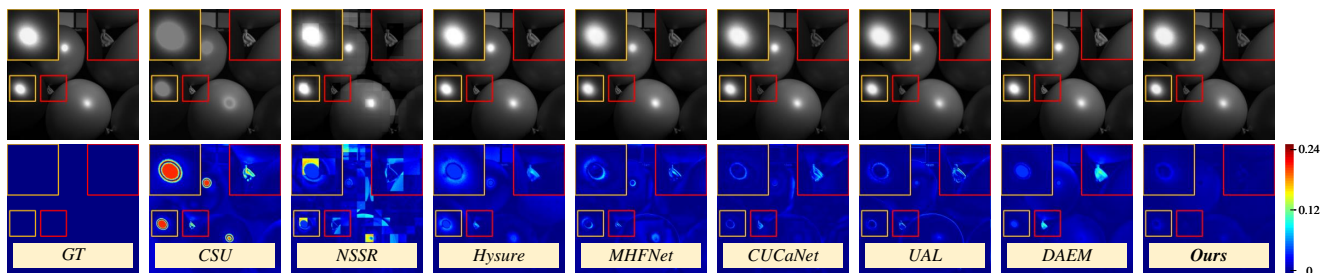


Figure 3. Visual reconstruction results and error images for the 11th band of the HR-HSI images from the CAVE dataset.

	Configurations	PSNR \uparrow	SSIM \uparrow	SAM \downarrow	ERGAS \downarrow
1	w/o \mathcal{L}_{MC}	37.33	0.975	10.04	0.71
	w/o attract	39.95	0.984	7.82	0.51
	w/o repel	38.79	0.981	8.56	0.60
2	concat & conv	39.89	0.984	9.55	0.55
	cross	<u>40.17</u>	<u>0.987</u>	<u>7.38</u>	0.52
3	w/o \mathcal{L}_{MCT}	39.83	0.984	7.73	0.54
	w/o \mathcal{L}_{MCT2}	40.13	0.985	7.71	<u>0.45</u>
4	conv DE	37.53	0.976	8.73	0.69
	Ours	42.05	0.990	6.57	0.42

Table 2. Ablation experiment results. The best results are in **bold**, while the second-best results are in underlined.

Methods	FLOPs (G)	Param (M)	Training Time (min)	Test Time (s)	Test Iterations
MHFNet [41]	21226	129.4	1340	21.36	1
CUCaNet[45]	7226	2.28	/	1806	10000
UAL [51]	3599	7.13	325	28.36	1500
DAEM [9]	1.67	0.02	119	<u>19.56</u>	<u>250</u>
Ours	<u>279.42</u>	<u>0.54</u>	<u>215</u>	0.15	1

Table 3. Efficiency comparison among different methods. The best results are in **bold**, while the second-best results are in underlined.

In addition, more visual comparison results are given in the Supplementary Materials.

4.4. Algorithmic Analysis

Computational Cost Analysis. We compare various metrics for evaluating computational performance in Table 3 based on the CAVE dataset. It is worth mentioning that some methods, like DAEM [9] and UAL [51], employ a fine-tuning strategy during inference, which necessitates several iterations to obtain optimal results. The number of iterations required during testing is listed in the last column of Table 3. As a result, the actual computational costs are significantly higher than the FLOPs for a single inference shown in the first column, which also accounts for why these algorithms are more time-consuming. Note that MossFuse retains only the multi-modality decoupling and modality reconstruction processes during inference, and requires just a single iteration to infer the HR-HSI, making it more computationally efficient and practical in comparison.

Degradation Estimation. We have selected several full-blind methods, such as Hysure [33] and DAEM [9], to compare the estimated degradation parameters in Fig. 7. Our algorithm nearly perfectly estimates the degradation parameters in both the spatial and spectral dimensions.

In addition, more comparison results about the degradation estimation are given in the Supplementary Materials.

Modality Decoupling Capability Analysis. To demonstrate the effectiveness of the modality decoupling, we visualize four key decoupled features: F_Y^S and F_x^S , representing the modality-shared representations, and F_Y^C and F_x^C , representing the modality-complementary representations of

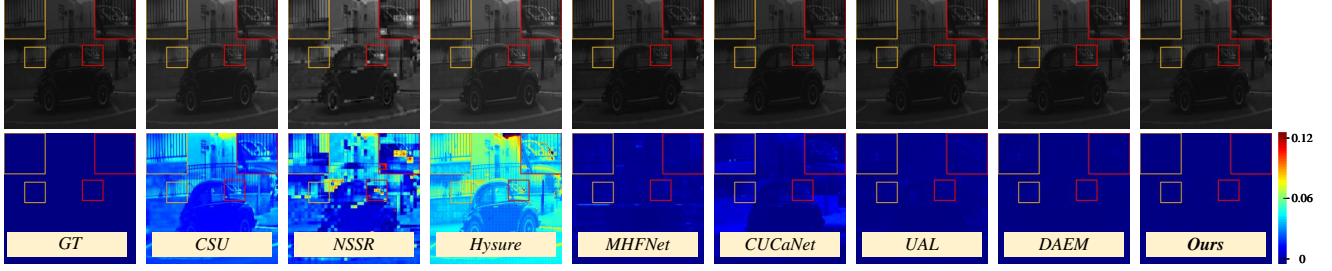


Figure 4. Visual reconstruction results and error images for the 11th band of the HR-HSI images from the NTIRE2018 dataset.

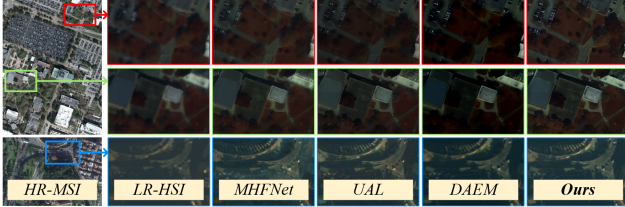


Figure 5. Visual reconstruction results from the NCALM (upper part) and WV-2 (bottom part) datasets. We show the images with 25-16-7 and 5-3-2 as R-G-B, respectively.

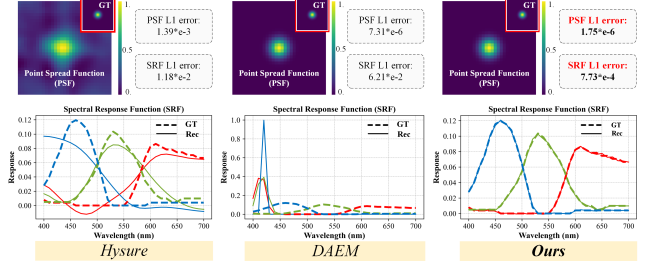


Figure 7. Comparison of degradation parameters PSF and SRF estimated by different methods.

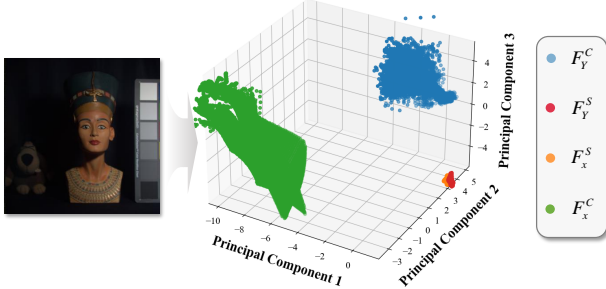


Figure 6. Data distribution of four decoupled features after PCA, showing the separation between modality-shared and modality-complementary representations.

spatial and spectral information, respectively. Specifically, we reduced the four features to three dimensions using Principal Component Analysis (PCA) and represented them in a spatial coordinate system, as shown in Fig. 6. The data distributions of two modality-shared features are compact and consistent, while they are clearly distinguishable from the distributions of the modality-complementary spatial and spectral features. This highlights the effective modality decoupling capability of our MossFuse.

Ablation Study. As shown in Table 2, we conduct comprehensive ablation studies using the CAVE dataset to validate the influence of four critical components in MossFuse. **1.Modality Clustering Loss.** We first remove the \mathcal{L}_{MC} to access its contribution, denoted as 'w/o \mathcal{L}_{MC} '. In addition, we modify the \mathcal{L}_{MC} by separately removing the attraction term and the repulsion term from the loss, la-

beled as 'w/o attract' and 'w/o repel,' respectively. Specifically, the modified modality clustering loss can be formulated by $\mathcal{L}'_{MC} = \log(f(F_Y^C, F_x^C) + \sum_{i \in \{Y, x\}} f(F_i^S, F_i^C))$ and $\mathcal{L}''_{MC} = -\log(f(F_Y^S, F_x^S))$, respectively, where $f(a, b) = \exp^{\cos(a, b)}$ represents the latent space similarity metric, which measures the cosine similarity between a and b . The dropped performance in Table 2 confirms the effort of the modality clustering loss. **2.Modality Aggregation block.** We replace both the spatial- and spectral-modality aggregation block with simpler fusion methods: concatenation followed by convolution and cross-attention, denoted as 'concat&conv' and 'cross,' respectively. The results in Table 2 show that these simpler fusion strategies are insufficient for adequately merging the information from both modalities. **3.Modality constraint process.** We evaluate the effectiveness of the modality constraint process by removing it entirely or by only removing the supervision branch for modality-shared representations, which means the modality constraint loss retains only term \mathcal{L}_{MCT1} . These scenarios are labeled as 'w/o \mathcal{L}_{MCT} ' and 'w/o \mathcal{L}_{MCT2} ', respectively. The performance decline observed in Table 2 confirms the importance of this component. **4.Degradation Estimation Process.** We replace the explicit degradation estimation with general convolution layers without constraints, referred to as 'conv DE.' The inferior performance in Table 2 demonstrates the significance of the proposed degradation estimation process.

In addition, more comparison results of ablation studies are given in the Supplementary Materials.

5. Conclusion

In this paper, we show that modality decoupling is essential for hyperspectral image fusion. Specifically, we propose a simple framework that decouples the modality-shared/complementary components and aggregates the concise representation of the LR-HSI and HR-MSI to reduce the modality redundancy. Also, we proposed a modality clustering loss to guide the network to aggregate the shared information while distinguishing it from its modality-complementary components. Extensive experiments prove that fusing the decoupled modality-shared LR-MSI and modality-complementary spatial and spectral information enhances fusion performance without the need for complex architecture or vast parameters, leading to a finer HR-HSI with fewer parameters and inference time.

References

- [1] Boaz Arad, Ohad Ben-Shahar, and Radu Timofte. Ntire 2018 challenge on spectral reconstruction from rgb images. In *Proceedings of the IEEE Conference on Computer Vision and Pattern Recognition Workshops*, pages 929–938, 2018. 6, 7
- [2] Ayan Chakrabarti and Todd Zickler. Statistics of real-world hyperspectral images. In *CVPR 2011*, pages 193–200. IEEE, 2011. 6, 7
- [3] Zheng Chen, Yulun Zhang, Jinjin Gu, Linghe Kong, Xiaokang Yang, and Fisher Yu. Dual aggregation transformer for image super-resolution. In *Proceedings of the IEEE/CVF international conference on computer vision*, pages 12312–12321, 2023. 4
- [4] Shangqi Deng, Liang-Jian Deng, Xiao Wu, Ran Ran, and Rui Wen. Bidirectional dilation transformer for multispectral and hyperspectral image fusion. In *IJCAI*, pages 3633–3641, 2023. 3
- [5] Renwei Dian, Leyuan Fang, and Shutao Li. Hyperspectral image super-resolution via non-local sparse tensor factorization. In *Proceedings of the IEEE Conference on Computer Vision and Pattern Recognition*, pages 5344–5353, 2017. 3
- [6] Weisheng Dong, Fazu Fu, Guangming Shi, Xun Cao, Jinjian Wu, Guangyu Li, and Xin Li. Hyperspectral image super-resolution via non-negative structured sparse representation. *IEEE Transactions on Image Processing*, 25(5):2337–2352, 2016. 6, 7
- [7] Xiyu Fu, Sen Jia, Meng Xu, Jun Zhou, and Qingquan Li. Fusion of hyperspectral and multispectral images accounting for localized inter-image changes. *IEEE Transactions on Geoscience and Remote Sensing*, 60:1–18, 2021. 3
- [8] Jinjin Gu, Hannan Lu, Wangmeng Zuo, and Chao Dong. Blind super-resolution with iterative kernel correction. In *Proceedings of the IEEE/CVF conference on computer vision and pattern recognition*, pages 1604–1613, 2019. 5
- [9] Wen-jin Guo, Weiyang Xie, Kai Jiang, Yunsong Li, Jie Lei, and Leyuan Fang. Toward stable, interpretable, and lightweight hyperspectral super-resolution. In *Proceedings of the IEEE/CVF Conference on Computer Vision and Pattern Recognition*, pages 22272–22281, 2023. 3, 6, 7
- [10] Xiaolin Han, Jing Yu, Jing-Hao Xue, and Weidong Sun. Hyperspectral and multispectral image fusion using optimized twin dictionaries. *IEEE Transactions on Image Processing*, 29:4709–4720, 2020. 3
- [11] Jie Hu, Li Shen, and Gang Sun. Squeeze-and-excitation networks. In *Proceedings of the IEEE conference on computer vision and pattern recognition*, pages 7132–7141, 2018. 4, 5
- [12] Qian Hu, Xinya Wang, Junjun Jiang, Xiao-Ping Zhang, and Jiayi Ma. Exploring the spectral prior for hyperspectral image super-resolution. *IEEE Transactions on Image Processing*, 2024. 1
- [13] Jun Jiang, Dengyu Liu, Jinwei Gu, and Sabine Süsstrunk. What is the space of spectral sensitivity functions for digital color cameras? In *2013 IEEE Workshop on Applications of Computer Vision (WACV)*, pages 168–179. IEEE, 2013. 6
- [14] Charilaos I Kanatsoulis, Xiao Fu, Nicholas D Sidiropoulos, and Wing-Kin Ma. Hyperspectral super-resolution: A coupled tensor factorization approach. *IEEE Transactions on Signal Processing*, 66(24):6503–6517, 2018. 3
- [15] Rei Kawakami, Yasuyuki Matsushita, John Wright, Moshe Ben-Ezra, Yu-Wing Tai, and Katsushi Ikeuchi. High-resolution hyperspectral imaging via matrix factorization. In *CVPR 2011*, pages 2329–2336. IEEE, 2011. 3
- [16] Diederik P Kingma and Jimmy Ba. Adam: A method for stochastic optimization. *arXiv preprint arXiv:1412.6980*, 2014. 6
- [17] Charis Lanaras, Emmanuel Baltsavias, and Konrad Schindler. Hyperspectral super-resolution by coupled spectral unmixing. In *Proceedings of the IEEE international conference on computer vision*, pages 3586–3594, 2015. 6, 7
- [18] Jiaojiao Li, Songcheng Du, Rui Song, Chaoxiong Wu, Yunsong Li, and Qian Du. Hasic-net: Hybrid attentional convolutional neural network with structure information consistency for spectral super-resolution of rgb images. *IEEE Transactions on Geoscience and Remote Sensing*, 60:1–15, 2022. 1
- [19] Jiaojiao Li, Songcheng Du, Chaoxiong Wu, Yihong Leng, Rui Song, and Yunsong Li. Dr-cr net: Dense residual channel re-calibration network with non-local purification for spectral super resolution. In *Proceedings of the IEEE/CVF conference on computer vision and pattern recognition*, pages 1259–1268, 2022. 1
- [20] Jiaojiao Li, Songcheng Du, Rui Song, Yunsong Li, and Qian Du. Progressive spatial information-guided deep aggregation convolutional network for hyperspectral spectral super-resolution. *IEEE Transactions on Neural Networks and Learning Systems*, 2023. 6
- [21] Jiaxin Li, Ke Zheng, Lianru Gao, Li Ni, Min Huang, and Jocelyn Chanussot. Model-informed multi-stage unsupervised network for hyperspectral image super-resolution. *IEEE Transactions on Geoscience and Remote Sensing*, 2024. 5
- [22] Shutao Li, Renwei Dian, Leyuan Fang, and José M Bioucas-Dias. Fusing hyperspectral and multispectral images via coupled sparse tensor factorization. *IEEE Transactions on Image Processing*, 27(8):4118–4130, 2018. 3

- [23] Shutao Li, Renwei Dian, and Haibo Liu. Learning the external and internal priors for multispectral and hyperspectral image fusion. *Science China Information Sciences*, 66(4): 140303, 2023. 3
- [24] Xingyuan Li, Yang Zou, Jinyuan Liu, Zhiying Jiang, Long Ma, Xin Fan, and Risheng Liu. From text to pixels: A context-aware semantic synergy solution for infrared and visible image fusion. *arXiv preprint arXiv:2401.00421*, 2023. 3
- [25] Jie Lian, Lizhi Wang, Lin Zhu, Renwei Dian, Zhiwei Xiong, and Hua Huang. Physics-inspired degradation models for hyperspectral image fusion. *arXiv preprint arXiv:2402.02411*, 2024. 5
- [26] Chia-Hsiang Lin, Shih-Hsiu Huang, Ting-Hsuan Lin, and Pin Chieh Wu. Metasurface-empowered snapshot hyperspectral imaging with convex/deep (code) small-data learning theory. *Nature communications*, 14(1):6979, 2023. 1
- [27] Jianjun Liu, Zebin Wu, Liang Xiao, and Xiao-Jun Wu. Model inspired autoencoder for unsupervised hyperspectral image super-resolution. *IEEE Transactions on Geoscience and Remote Sensing*, 60:1–12, 2022. 5
- [28] Jinyuan Liu, Xingyuan Li, Zirui Wang, Zhiying Jiang, Wei Zhong, Wei Fan, and Bin Xu. Promptfusion: Harmonized semantic prompt learning for infrared and visible image fusion. *IEEE/CAA Journal of Automatica Sinica*, 12:1–14, 2024. 3
- [29] Qing Ma, Junjun Jiang, Xianming Liu, and Jiayi Ma. Learning a 3d-cnn and transformer prior for hyperspectral image super-resolution. *Information Fusion*, 100:101907, 2023. 3
- [30] Ying Qu, Hairong Qi, and Chiman Kwan. Unsupervised sparse dirichlet-net for hyperspectral image super-resolution. In *Proceedings of the IEEE conference on computer vision and pattern recognition*, pages 2511–2520, 2018. 3
- [31] Ran Ran, Liang-Jian Deng, Tian-Jing Zhang, Jianlong Chang, Xiao Wu, and Qi Tian. Knlconv: Kernel-space non-local convolution for hyperspectral image super-resolution. *IEEE Transactions on Multimedia*, 2024. 3
- [32] Kai Ren, Weiwei Sun, Xiangchao Meng, Gang Yang, Jiangtao Peng, and Jingfeng Huang. A locally optimized model for hyperspectral and multispectral images fusion. *IEEE Transactions on Geoscience and Remote Sensing*, 60:1–15, 2021. 3
- [33] Miguel Simoes, José Bioucas-Dias, Luis B Almeida, and Jocelyn Chanussot. A convex formulation for hyperspectral image superresolution via subspace-based regularization. *IEEE Transactions on Geoscience and Remote Sensing*, 53(6):3373–3388, 2014. 6, 7
- [34] Lucien Wald. Quality of high resolution synthesised images: Is there a simple criterion? In *Third conference" Fusion of Earth data: merging point measurements, raster maps and remotely sensed images"*, pages 99–103. SEE/URISCA, 2000. 6
- [35] Lucien Wald. *Data fusion: definitions and architectures: fusion of images of different spatial resolutions*. Presses des MINES, 2002. 6
- [36] Xinya Wang, Qian Hu, Yingsong Cheng, and Jiayi Ma. Hyperspectral image super-resolution meets deep learning: A survey and perspective. *IEEE/CAA Journal of Automatica Sinica*, 10(8):1668–1691, 2023. 1
- [37] Yinjian Wang, Wei Li, Yuanyuan Gui, Qian Du, and James E Fowler. A generalized tensor formulation for hyperspectral image super-resolution under general spatial blurring. *arXiv preprint arXiv:2409.18731*, 2024. 5
- [38] Zhou Wang, Alan C Bovik, Hamid R Sheikh, and Eero P Simoncelli. Image quality assessment: from error visibility to structural similarity. *IEEE Transactions on Image Processing*, 13(4):600–612, 2004. 6
- [39] Zhengjue Wang, Bo Chen, Ruiying Lu, Hao Zhang, Hongwei Liu, and Pramod K Varshney. Fusionnet: An unsupervised convolutional variational network for hyperspectral and multispectral image fusion. *IEEE Transactions on Image Processing*, 29:7565–7577, 2020. 1
- [40] Chanyue Wu, Dong Wang, Yunpeng Bai, Hanyu Mao, Ying Li, and Qiang Shen. Hsr-diff: Hyperspectral image super-resolution via conditional diffusion models. In *Proceedings of the IEEE/CVF International Conference on Computer Vision*, pages 7083–7093, 2023. 1
- [41] Qi Xie, Minghao Zhou, Qian Zhao, Deyu Meng, Wangmeng Zuo, and Zongben Xu. Multispectral and hyperspectral image fusion by ms/hs fusion net. In *Proceedings of the IEEE/CVF Conference on Computer Vision and Pattern Recognition*, pages 1585–1594, 2019. 6, 7
- [42] Yonghao Xu, Bo Du, Liangpei Zhang, Daniele Cerra, Miguel Pato, Emiliano Carmona, Saurabh Prasad, Naoto Yokoya, Ronny Hänsch, and Bertrand Le Saux. Advanced multi-sensor optical remote sensing for urban land use and land cover classification: Outcome of the 2018 ieee grss data fusion contest. *IEEE Journal of Selected Topics in Applied Earth Observations and Remote Sensing*, 12(6):1709–1724, 2019. 6
- [43] Yang Xu, Zebin Wu, Jocelyn Chanussot, and Zhihui Wei. Hyperspectral images super-resolution via learning high-order coupled tensor ring representation. *IEEE transactions on neural networks and learning systems*, 31(11):4747–4760, 2020. 3
- [44] Pei Yang, Yong Ma, Xiaoguang Mei, Qihai Chen, Minghui Wu, and Jiayi Ma. Deep blind super-resolution for hyperspectral images. *Pattern Recognition*, 157:110916, 2025. 1
- [45] Jing Yao, Danfeng Hong, Jocelyn Chanussot, Deyu Meng, Xiaoxiang Zhu, and Zongben Xu. Cross-attention in coupled unmixing nets for unsupervised hyperspectral super-resolution. In *Computer Vision–ECCV 2020: 16th European Conference, Glasgow, UK, August 23–28, 2020, Proceedings, Part XXIX 16*, pages 208–224. Springer, 2020. 3, 6, 7
- [46] Fumihito Yasuma, Tomoo Mitsunaga, Daisuke Iso, and Shree K Nayar. Generalized assorted pixel camera: post-capture control of resolution, dynamic range, and spectrum. *IEEE Transactions on Image Processing*, 19(9):2241–2253, 2010. 6, 7
- [47] Fei Ye, Zebin Wu, Xiuping Jia, Jocelyn Chanussot, Yang Xu, and Zhihui Wei. Bayesian nonlocal patch tensor factorization for hyperspectral image super-resolution. *IEEE Transactions on Image Processing*, 2023. 3
- [48] Zongsheng Yue, Qian Zhao, Jianwen Xie, Lei Zhang, Deyu Meng, and Kwan-Yee K Wong. Blind image super-resolution

- with elaborate degradation modeling on noise and kernel. In *Proceedings of the IEEE/CVF conference on computer vision and pattern recognition*, pages 2128–2138, 2022. 5
- [49] Roberta H Yuhas, Alexander FH Goetz, and Joe W Boardman. Discrimination among semi-arid landscape endmembers using the spectral angle mapper (sam) algorithm. In *JPL, Summaries of the Third Annual JPL Airborne Geoscience Workshop. Volume 1: AVIRIS Workshop*, 1992. 6
- [50] Syed Waqas Zamir, Aditya Arora, Salman Khan, Munawar Hayat, Fahad Shahbaz Khan, and Ming-Hsuan Yang. Restormer: Efficient transformer for high-resolution image restoration. In *Proceedings of the IEEE/CVF conference on computer vision and pattern recognition*, pages 5728–5739, 2022. 3
- [51] Lei Zhang, Jiangtao Nie, Wei Wei, and Yanning Zhang. Unsupervised test-time adaptation learning for effective hyperspectral image super-resolution with unknown degeneration. *IEEE Transactions on Pattern Analysis and Machine Intelligence*, 2024. 3, 6, 7
- [52] Mingjin Zhang, Chi Zhang, Qiming Zhang, Jie Guo, Xinbo Gao, and Jing Zhang. Essaformer: Efficient transformer for hyperspectral image super-resolution. In *Proceedings of the IEEE/CVF International Conference on Computer Vision*, pages 23073–23084, 2023. 1
- [53] Yiyuan Zhang, Xiaohan Ding, and Xiangyu Yue. Scaling up your kernels: Large kernel design in convnets towards universal representations. *arXiv preprint arXiv:2410.08049*, 2024. 3
- [54] Yang Zou, Xingyuan Li, Zhiying Jiang, and Jinyuan Liu. Enhancing neural radiance fields with adaptive multi-exposure fusion: A bilevel optimization approach for novel view synthesis. In *Proceedings of the AAAI Conference on Artificial Intelligence*, pages 7882–7890, 2024. 3

Modality Decoupling is All You Need: A Simple Solution for Unsupervised Hyperspectral Image Fusion

Supplementary Material

A. Overview

As mentioned in the main body of our manuscript, this supplementary material includes an in-depth exploration of the network architecture, covering the Spectral-wise Transformer (SWT), Spectral-wise Self-attention (SWSA), LK-CNN, Spatial Attention (SA), and Channel Attention (CA). Additionally, it provides further comparisons on degradation estimation including the point spread function (PSF) and spectral response function (SRF), and presents additional visual results from our comparative analysis.

B. Network Architecture

B.1. Spectral-wise Transformer

As illustrated in Fig. 8(a), SWT consists of a Spectral-wise Self-attention (SWSA) module, a Feed-forward network, and two Layer Norm layers, along with several residual connections. Concretely, denotes $Z_{in} \in \mathbb{R}^{H \times W \times C}$ as the input feature embeddings of the SWT, where H and W represent the spatial size and C is the number of channels. The overall processing can be expressed as:

$$\begin{aligned} Z' &= SWSA(LN(Z_{in})) + Z_{in}, \\ Z_{out} &= FFN(LN(Z')), \end{aligned} \quad (8)$$

where $SWSA(\cdot)$, $FFN(\cdot)$, and $LN(\cdot)$ represent the SWSA module, Feed-forward network, and Layer Norm layer, and Z_{out} denotes the output feature embeddings.

In addition, as shown in Fig. 8(b), SWSA is designed to capture long-range dependencies of input features that exhibit spectral correlations. To be specific, given the input feature $F_{in} \in \mathbb{R}^{H \times W \times C}$, we first leverage three linear projection layers to generate the query (Q), key (K) and value (V) matrices, respectively. Subsequently, we split Q , K , and V into J heads along the spectral dimension. Note that SWSA treats each spectral as an individual token, thus, the spectral-wise attention map $\mathbf{Att}_j \in \mathbb{R}^{C \times C}$ of $head_j$ can be formulated as:

$$\mathbf{Att}_j = \text{softmax}(K_j^T Q_j / d_j), \quad (9)$$

where \mathbf{T} represents the transposed operation, d_j is a learnable temperature parameter, $j \in [1, J]$. Further, $head_j$ can be calculated as $head_j = V_j \mathbf{Att}_j$. Subsequently, the outputs of J heads are concatenated and then passed through a linear projection to produce the final output of the SWSA.

B.2. LK-CNN

As illustrated in Fig. 8(c), the LK-CNN block consists of a Dilated Reparam Block, an SE Block, a Feed-forward network, and several Batch Normalization (BN) layers. To balance computational efficiency and effectiveness, the Dilated Reparam Block employs dilated small-kernel convolutional layers to augment a non-dilated large-kernel convolutional layer. These dilated layers are parameter-equivalent to a non-dilated convolutional layer with a larger sparse kernel, enabling the entire block to be equivalently transformed into a single large-kernel convolution.

Specifically, the Dilated Reparam Block includes a series of depth-wise dilated convolutional layers operating in parallel with different kernel sizes and dilation rates. The outputs of both layers are combined after their respective Batch Normalization (BN) layers. During the training phase, the parameters of the small-kernel layer and its BN layers are merged into the large-kernel layer, resulting in a mathematically equivalent model. Post-merging, the final model retains only the large kernel, effectively eliminating the small kernels while preserving the original functionality.

B.3. Spatial Attention

As depicted in Fig. 8(d), the Spatial Attention (SA) mechanism is designed to enhance the model's focus on informative regions within the input features by generating a spatial attention map. For an input feature $F^{spa} \in \mathbb{R}^{H \times W \times C}$, the spatial attention map is produced by first processing the input through three 1×1 convolutional layers. These layers reduce the channel dimension to 1, resulting in a spatially-aware map $F_{Att}^{spa} \in \mathbb{R}^{H \times W \times 1}$. A sigmoid activation function is then applied to ensure the values in F_{Att}^{spa} lie between 0 and 1, effectively serving as weights to emphasize the importance of different spatial locations.

B.4. Channel Attention

As shown in Fig. 8(e), Channel Attention (CA) is designed to enhance feature representation by focusing on the most critical channels of a feature map. Given an input feature map $F^{spe} \in \mathbb{R}^{H \times W \times C}$, the CA module first aggregates global spatial information for each channel using a Global Average Pooling (GAP) layer, reducing the spatial dimensions to 1×1 while preserving the channel-wise information. After pooling, the resulting vector is passed through three 1×1 convolutional layers with a bottleneck to model channel dependencies and interactions. Finally, a sigmoid activation function is applied to the output, producing nor-

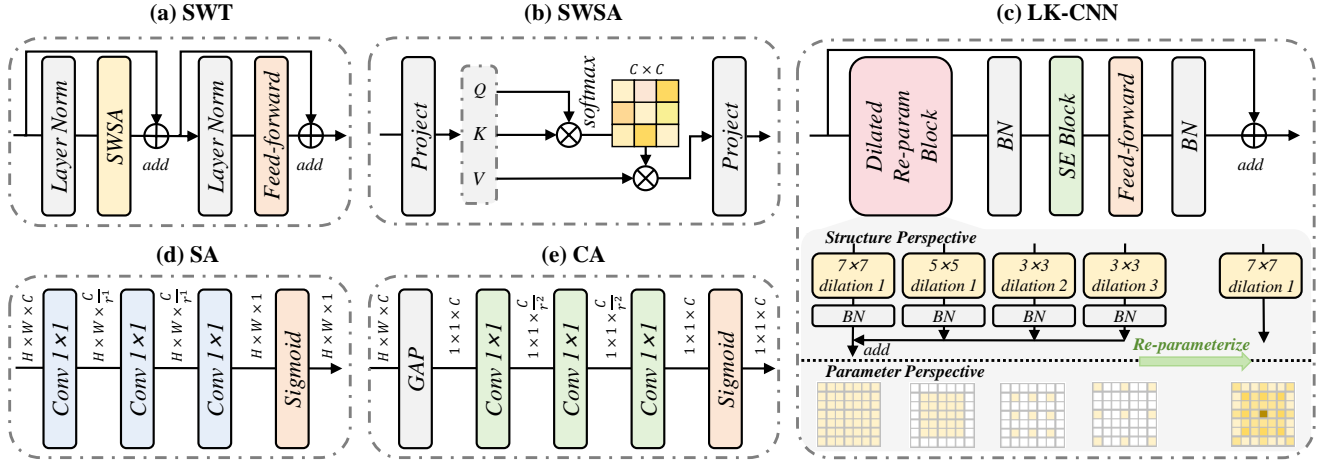


Figure 8. The detailed network architecture of (a) SWT, (b) SWSA, (c) LK-SNN, (d) SA, and (e) CA.

malized weights between 0 and 1 that represent the relative importance of each channel.

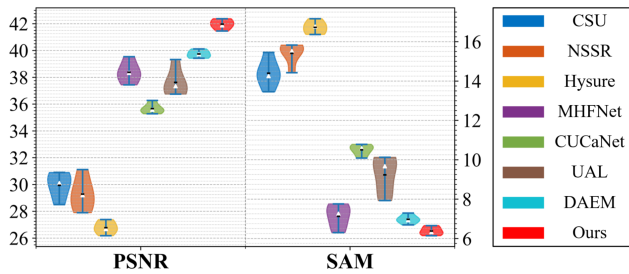


Figure 9. The distribution of two measurement metrics (PSNR, SAM) for the different methods under various degradations. The black lines and the white triangles denote medium and mean values.

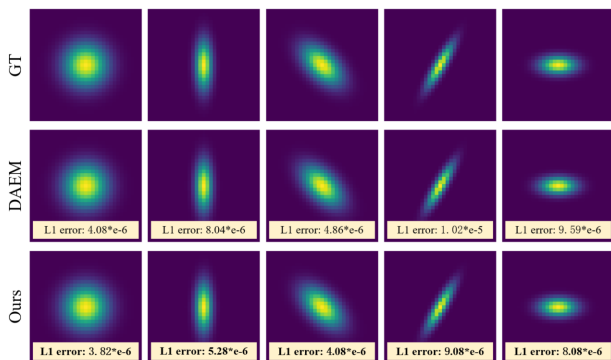


Figure 10. Comparison of PSF estimated by different methods.

C. Comparison on Degradation Estimation

For unsupervised hyperspectral and multispectral image fusion tasks, the absence of ground truth means that the accuracy of the degradation model estimation directly impacts

the precision of HR-HSI reconstruction. To evaluate the framework’s robustness in estimating degradation parameters under another five groups of degradation conditions, using the CAVE dataset, we compared it with the DAEM algorithm. As shown in Fig.10 and Fig. 11, our method achieves more accurate estimates of the degradation parameters, particularly for the SRF. Furthermore, we present in Fig.9 the distribution of two evaluation metrics (PSNR and SAM) for reconstruction results across various degradation conditions. These results highlight our algorithm’s superior performance and robustness compared to others.

D. Visual Results of Ablation Study

To visually compare the reconstruction results from different ablation experiments, as shown in Fig. 13, by leveraging the CAVE dataset, we first examined the error images of various methods. It is evident that any modification to ‘Ours’ results in a decrease in reconstruction accuracy. Additionally, to offer a more intuitive visualization of the error magnitude, as shown in Fig. 12, we displayed the error image of a specific band in a 3D coordinate space, where our algorithm once again outperformed the alternatives.

E. Visual Results of Comparison Results

We first show the visual reconstruction result of different algorithms based on the Harvard dataset in Fig. 15. In addition, to provide a more intuitive demonstration of the spectral recovery accuracy of different algorithms, we display the reconstructed spectral values from several positions in an image on three synthetic datasets, as shown in Fig. 14. Moreover, we provide some visualizations of reconstruction errors for different algorithms across three datasets, as shown in Fig. 16, Fig. 17, and Fig. 18. All in all, our algorithm achieves the best reconstruction visual results.

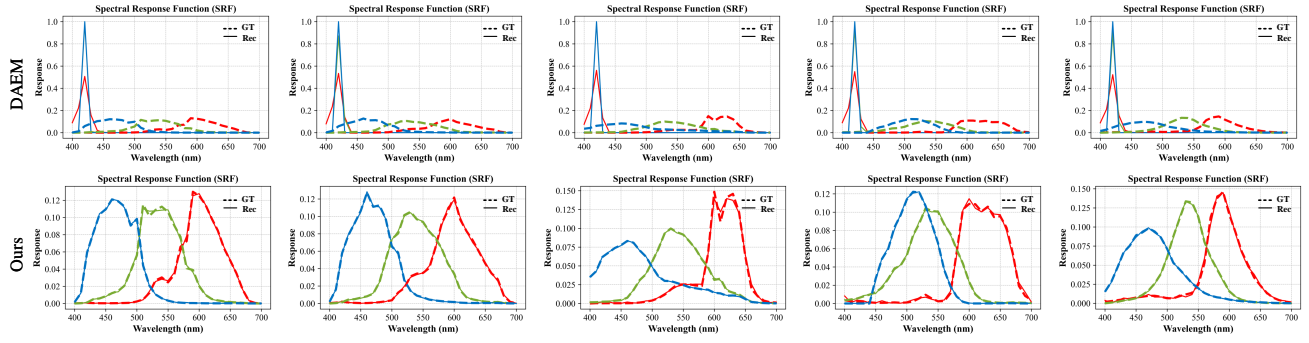


Figure 11. Comparison of SRF estimated by different algorithms.

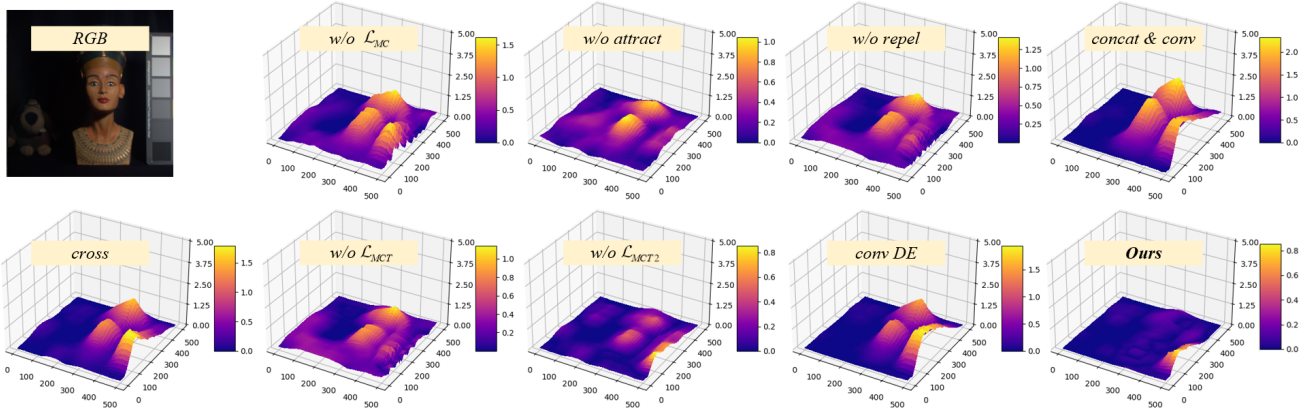


Figure 12. The reconstruction error comparison for the 8th band of the HR-HSIs from the CAVE dataset using different ablation experiments.

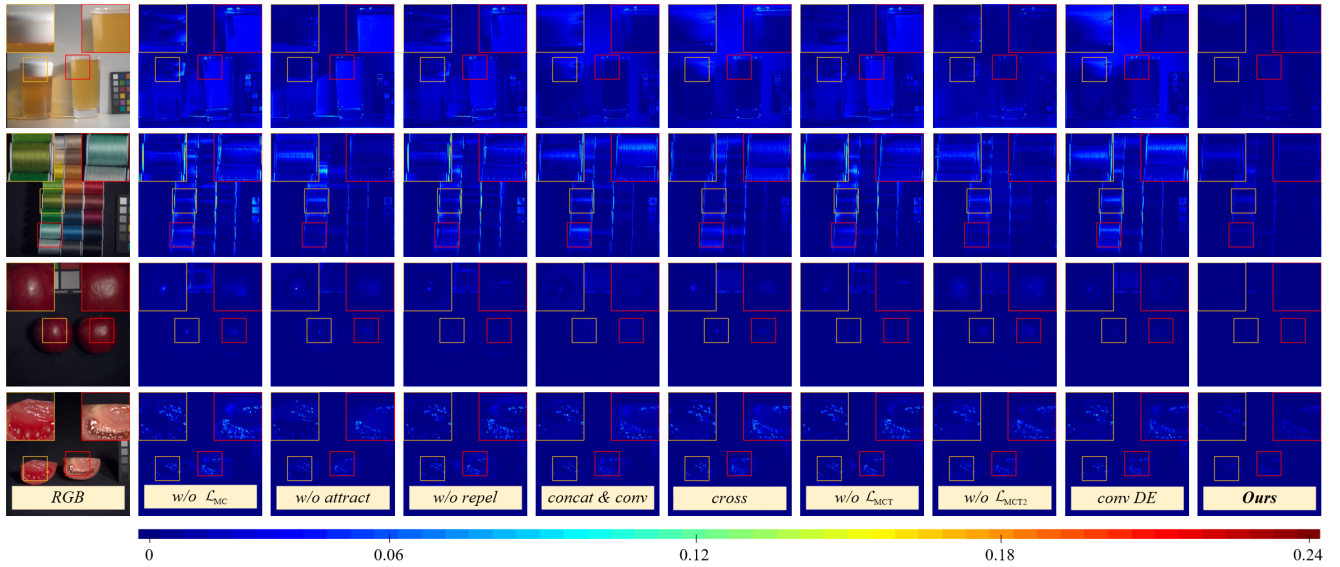


Figure 13. The reconstruction error comparison for the 11th band of the HR-HSIs from the CAVE dataset of ablation experiments.

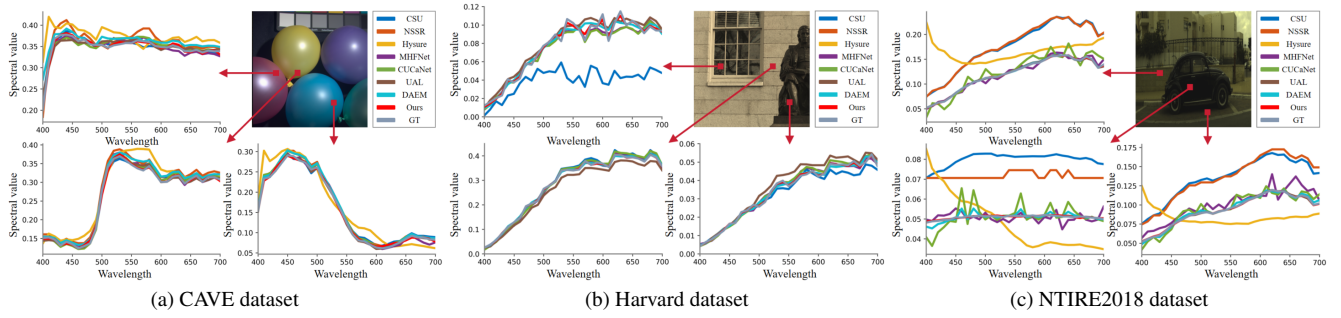


Figure 14. Comparison of reconstructed spectra curves in CAVE, Harvard, and NTIRE2018 datasets.

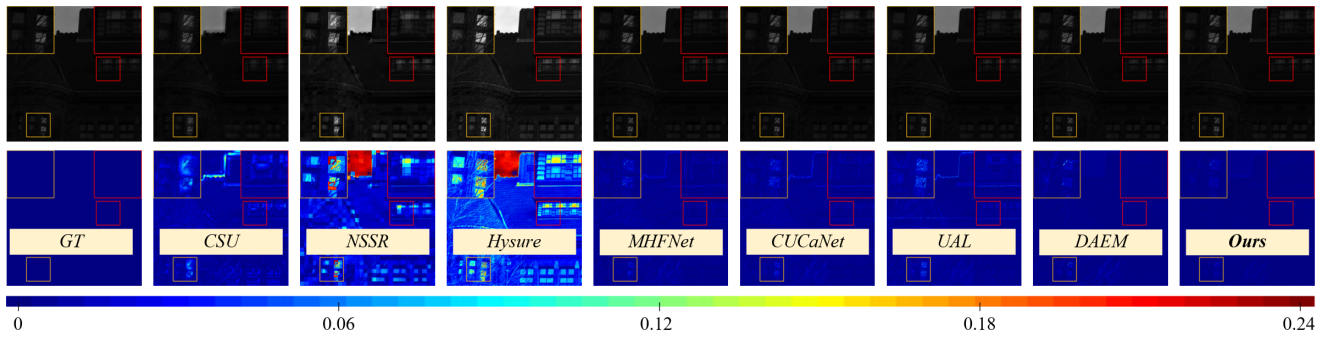


Figure 15. Visual reconstruction results and error images for the 11th band of the HR-HSI images from the Harvard dataset.

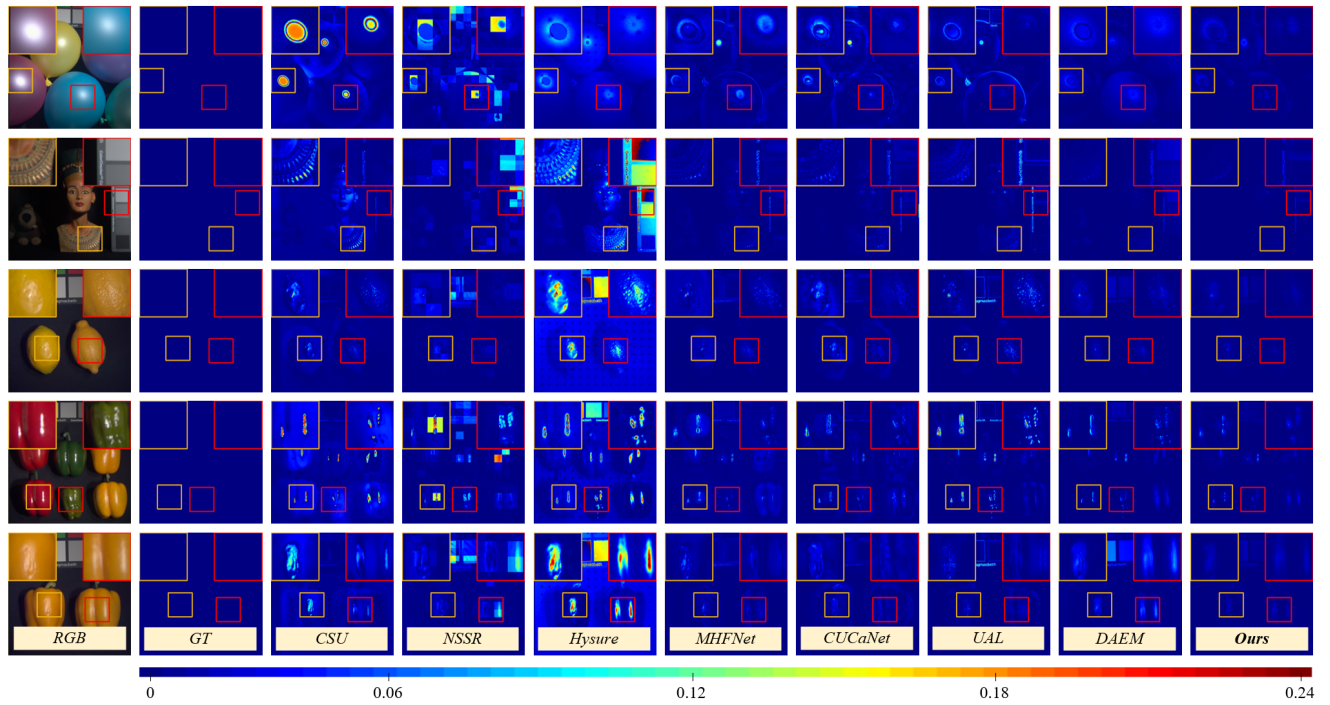


Figure 16. The reconstruction error comparison for the 8th band of the HR-HSIs from the CAVE dataset using different algorithms.

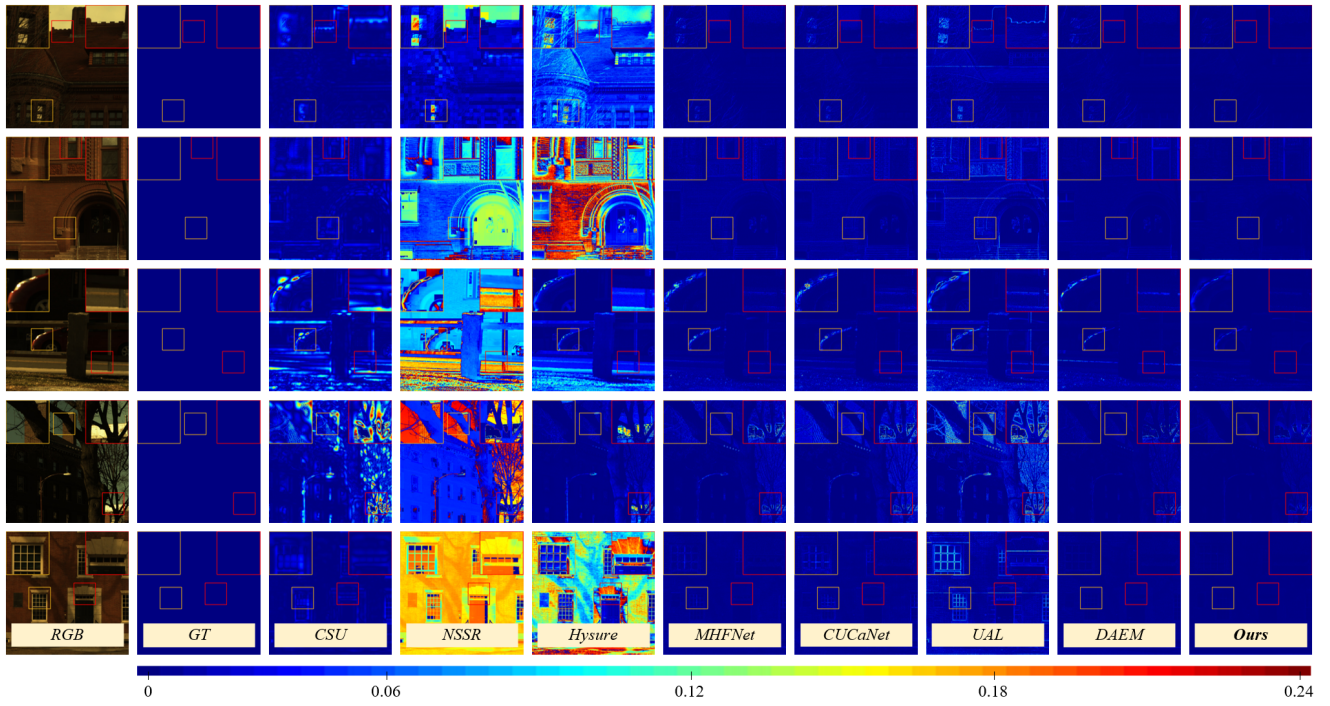


Figure 17. The reconstruction error comparison for the 18th band of the HR-HSIs from the Harvard dataset using different algorithms.

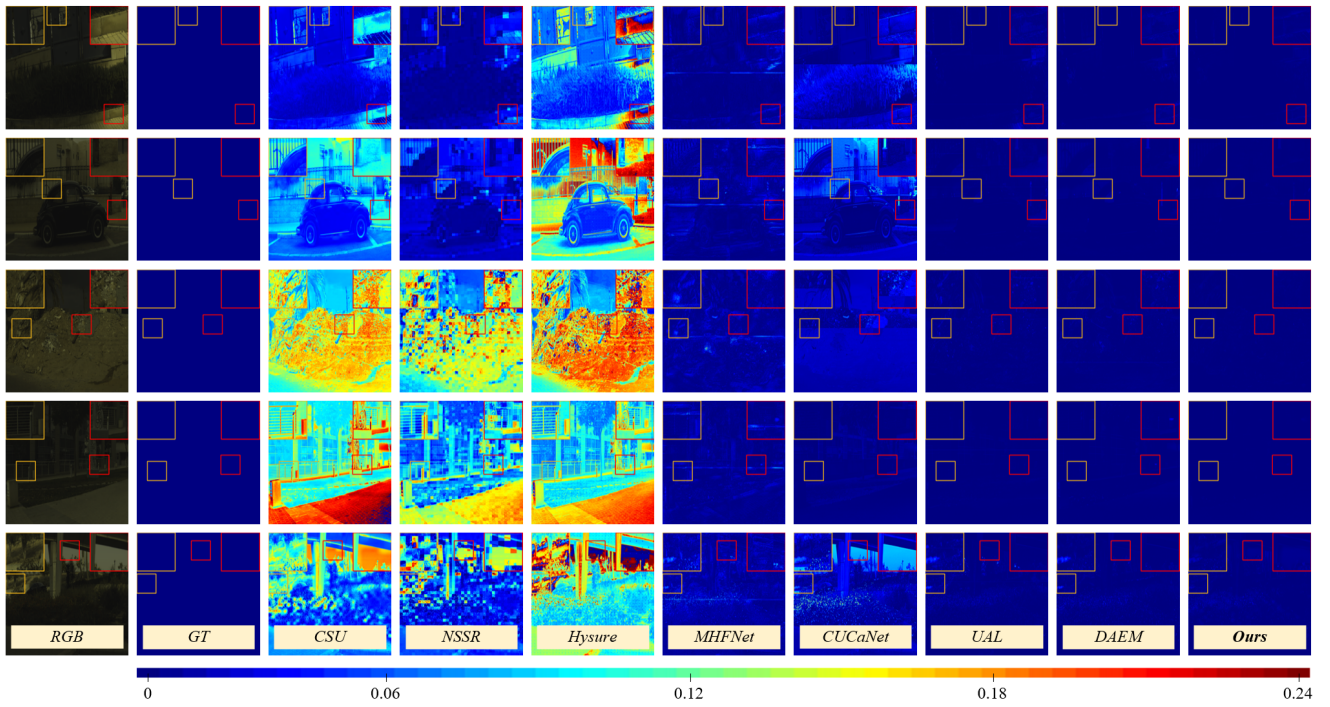


Figure 18. The reconstruction error comparison for the 28th band of the HR-HSIs from the NTIRE2018 dataset using different algorithms.